R-free factor and experimental charge-density analysis of 1-(2′-aminophenyl)-2-methyl-4-nitro-imidazole: a crystal structure with Z′ = 2

**Agnieszka Paul,[a,b] Maciej
Kubicki,[a]* Christian Jelsch,[b]*
Pierrick Durand[b] and Claude
Lecomte[b]**

[a]Faculty of Chemistry, Adam Mickiewicz
University, Grunwaldzka 6, 60-780 Poznań,
Poland, and [b]Cristallographie, Résonance
Magnétique et Modelisations CRM2, UMR
UHP-CNRS 7036, Institut Jean Barriol, Nancy
Université, BP 70239, 54506 Vandoeuvre-les-
Nancy, France

Correspondence e-mail: mkubicki@amu.edu.pl,
christian.jelsch@crm2.uhp-nancy.fr

The experimental charge-density distribution was determined for 1-(2′-aminophenyl)-2-methyl-4-nitro-1H-imidazole crystals. An anharmonic model was applied to the N atoms of both amino groups and to one nitro group in order to account for high residual peaks after harmonic multipole refinement and to obtain a better charge-density model. Free R-factor calculations [Brünger (1992). Nature, **355**, 472–475] with restrained models implemented in MoPro were used to determine the degree of similarity of the two symmetry-independent molecules in the unit cell. The results are compared with 1-phenyl-4-nitroimidazole in order to analyze the influence of the amine and methyl functional groups. The asymmetric unit contains two symmetry-independent molecules giving rise to a dimer connected via strong N—H···N hydrogen bonds; these dimers are the building blocks of the crystal. In the crystal structure there are also weaker interactions and many short directional contacts (C—H···O, C—H···N and C—H···π), for which the Koch–Popelier topological criteria were applied. This analysis revealed that the C—H···π interactions lie at the border between weak hydrogen bonds and van der Waals interactions. Special attention was also paid to stabilizing H···H interactions. It turned out that the electron density, Laplacian and density energies at the critical points show an exponential dependence on the contact distance, similar to the relation found for other interactions.

1. Introduction

Nowadays experimental studies of the electron-density distribution in crystals are more rapidly accessible due to the availability of CCD detectors, which greatly enhances the speed of data collection and increases the redundancy of the resulting data sets. This improvement, together with the development of user-friendly software packages for pseudo-atom multipolar refinement (Guillot, Viry et al., 2001; Jelsch et al., 2005; Volkov et al., 2006; Guillot, 2010), prompted charge-density analyses to become one of the most important methods for the experimental investigation of the fundamental properties of molecules. The method applies not only to small organic molecules (Guillot, Muzet et al., 2001; Bouhmaida et al., 2009), but also to biological macromolecules (e.g. Guillot et al., 2008), with the emphasis often put on intermolecular interactions, especially hydrogen bonds (Espinosa et al., 1999; Ranganathan et al., 2003; Hoser et al., 2009; Munshi & Row, 2006) or ligand–protein interactions (Muzet et al., 2003; Liebschner et al., 2009; Fournier et al., 2009).

Imidazole plays an important role in biological systems as the main constituent of histamine, histidine and purine bases

Table 1
Experimental details.

Crystal data	
Chemical formula	$C_{10}H_{10}N_4O_2$
M_r	218.22
Crystal system, space group	Monoclinic, $P2_1/c$
Temperature (K)	100
a, b, c (Å)	11.0299 (2), 10.0921 (2), 18.6365 (3)
β (°)	97.238 (2)
V (Å^3)	2057.99 (6)
Z	8
Radiation type	Mo $K\alpha$
μ (mm^{-1})	0.10
Crystal to detector distance (mm)	45
Crystal size (mm)	$0.35 \times 0.35 \times 0.35$
Data collection	
Diffractometer	Xcalibur, Eos
Absorption correction	Analytical
T_{min}, T_{max}	0.974, 0.979
No. of measured, independent and observed [$I > 2\sigma(I)$] reflections	26 440, 15 247, 15 219
R_{int}	0.033
Completeness (%) up to $s = 1\,13$ Å^{-1}	99.95
Refinement method IAM/multipole model	
No. of parameters IAM/multipole model	369/975
Weighting scheme:	
Spherical atom model	$w^{-1} = [\sigma^2(F_o)^2 + 0.0753P^2)$, where $P = (F_o^2 + 2F_c^2)/3$
Multipole atom model	$w^{-1} = a\sigma^2(F_o)^2$, where $a = 1.100$
Goodness-of-fit on F^2:	
Spherical atom model (*SHELXL*97)	1.05
Multipole atom model	1.07
Final $R(F)$ indices [$I > 2\sigma(I)$]:	
Spherical atom model	$R_1 = 0.049$, $wR_2 = 0.147$
Aspherical atom model	$R_1 = 0.030$, $wR_2 = 0.025$
$\Delta\rho_{max}$, $\Delta\rho_{min}$ (e Å^{-3}):	
Spherical atom model (sin $\theta/\lambda \le$ 1.16 Å^{-1})	0.91/−0.54
Multipole atom model (sin $\theta/\lambda \le$ 1.10 Å^{-1})	0.28/−0.22

(Epstein *et al.*, 1982). Its nitro derivatives are often used as antibiotic drugs, to combat anaerobic bacteria and parasitic infections (Edwards, 1981; Kulda & Hrdý, 2008). To the best of our knowledge, the experimental electron-density distribution has only been analyzed for crystals of imidazole itself (Epstein *et al.*, 1982; Stewart, 1991), histidine (Coppens *et al.*, 1999), 1,2-dimethyl-5-nitroimidazole (De Bondt *et al.*, 1991) and 1-phenyl-4-nitroimidazole (Kubicki *et al.*, 2002). The standard-resolution crystal structures of numerous 4-nitroimidazole derivatives – including the title compound, 1-(2′-amino-phenyl)-2-methyl-4-nitroimidazole, hereinafter referred to as (1) – have been investigated recently in our laboratory as part of ongoing studies into the different weak interactions in molecular crystals (Kubicki *et al.*, 2001; Kubicki, 2004*a*,*b*; Kubicki, 2005; Kubicki & Wagner, 2007, 2008; Wagner & Kubicki, 2007; Wagner *et al.*, 2007). The structure of 1-phenyl-4-nitroimidazole (Kubicki *et al.*, 2002) was the first of this group which was analyzed with the AIM (atoms-in-molecules) approach based on the topological analysis of the charge-density distribution (Bader, 1990). In this paper special attention was paid to the electron-withdrawing effect of the

nitro group and to the analysis of the weak C—H···O and C—H···N interactions.

Here we continue the investigation of the charge-density distribution in a crystal structure which consists of two chemically identical but symmetry-independent molecules of (1) (Fig. 1), which interact *via* N—H···N, N—H···O, C—H···O, C—H···N and C—H···π interactions. Average free R factors were calculated for models with different levels of restraints to find the degree of similarity. An anharmonic motion model was applied differently in the two molecules – one molecule requires both the nitro and the amino group to be refined with third order Gram–Charlier coefficients, while for the second molecule only the amino group is modeled in this way. Also, some arguments in favor of the presence of hydrogen–hydrogen interactions (as described in *e.g.* Matta *et al.*, 2003; Grabowski, 2006; Hernández-Trujillo & Matta, 2007) are discussed. A comparison with 1-phenyl-4-nitroimidazole (Kubicki *et al.*, 2002) should help to understand the influence of additional functional groups – methyl and amino ones – on the topological properties of the charge-density distribution.

2. Experimental

2.1. X-ray diffraction data collection

A yellowish cube-shaped crystal ($0.35 \times 0.35 \times 0.35$ mm) was used for data collection at 100 K on an Oxford Diffraction Xcalibur Eos four-circle diffractometer equipped with a CCD detector and graphite-monochromated Mo $K\alpha$ radiation. The temperature was controlled using an Oxford Instruments Cryosystem cooling device. A total of 1683 images were collected in 23 runs with different diffractometer angle settings chosen to obtain the high redundancy required for charge-density analysis. Diffraction data up to sin $\theta/\lambda =$ 1.16 Å^{-1} were collected using an ω-scan with a rotation width of $\Delta\omega = 1°$. Different exposure times were chosen for different 2θ settings of the detector: 10 s for $\theta = \pm7.32°$ and 60 s for $\theta =$ 76.64°.
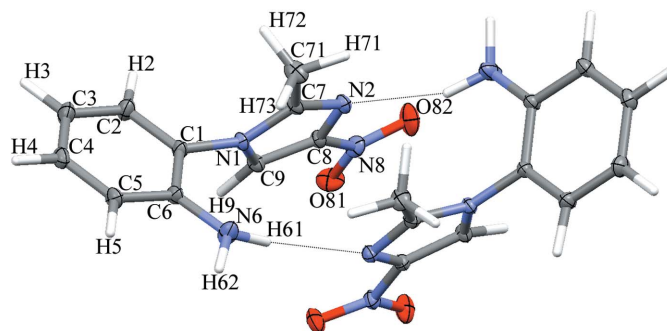

Figure 1
Anisotropic ellipsoid representation of the symmetry-independent molecules of (1) with atom-labeling scheme. Ellipsoids are drawn at the 50% probability level, H atoms are depicted as capped sticks (*MERCURY*; Macrae *et al.*, 2008). The labels of the second molecule are ordered in the same way and marked with an *A* (*e.g.* C1*A*, N1*A etc.*).

Details of the data collection together with crystallographic data are collected in Table 1.[1] The unit-cell parameters were determined by a least-squares fit to the 34 615 strongest reflections. Integration of the reflection intensities, data reduction and Lorentz-polarization corrections were carried out with *CrysAlis Red*, Version 171.33.36d (Oxford Diffraction, 2009). A numerical analytical absorption correction was applied using a multi-faced crystal model (Clark & Reid, 1995), and the data sorting and merging was performed with *SORTAV* (Blessing, 1987).

2.2. X-ray powder diffraction

The PXRD measurements were performed using a Panalytical X'Pert Pro diffractometer equipped with a Cu tube, a Ge(111) incident-beam monochromator ($\lambda = 1.5406$ Å) and an X'Celerator detector. Temperature-controlled diffractograms were collected with an Oxford cryostat (Oxford cryosystems Phenix) from 298 to 23 K (under vacuum, cooling rate of 6 K min^{-1}, 5 K increment, temperature stabilization 5 min). Data collection was carried out in the scattering angle range 2–55° with a 0.0167° step over 90 min.

The program *GSAS/EXGUI* (Larson & Von Dreele, 1994; Toby, 2001) was used for Le Bail extraction in the space group $P2_1/c$. Owing to the complexity of the structure and since powder X-ray diffraction (PXRD) is less sensitive than single-crystal measurements, single-crystal atomic parameters were simply used as the structural model. Only the cell dimensions, parameters of the pseudo-Voigt profile shape function and the zero shift were refined. Evolution of the cell parameters is shown in Fig. 2.

2.3. Least-squares refinements

The crystal structure was solved using *SIR*92 (Altomare *et al.*, 1993) and the IAM refinement was performed with *SHELXL*97 (Sheldrick, 2008). Non-H atoms were refined anisotropically and the anisotropic displacement parameters of H atoms were introduced at the final step using the *SHADE* server (Madsen, 2006). The structural results are in good agreement with those reported by Kubicki & Wagner (2008).

The charge density was subsequently refined against structure-factor amplitudes with the software *MoPro* (Guillot, Viry *et al.*, 2001; Jelsch *et al.*, 2005; Guillot, 2010) using the multipole Hansen–Coppens model (Hansen & Coppens, 1978) for pseudoatom electron density

$$\rho_{\text{atom}}(r) = \rho_{\text{core}}(r) + P_{\text{val}}\kappa^3 \rho_{\text{val}}(\kappa r) + \Sigma_l \kappa'^3 R_l(\kappa' r)\Sigma_m P_{lm\pm}(\theta, \varphi),$$
(1)

where the first two terms are the spherically averaged core and valence electron densities of the atom, and the last term corresponds to the non-spherical valence density which is described in terms of real spherical harmonic functions. P_{val} is the valence population, $P_{lm\pm}$ are the multipole populations,

and κ and κ' are the contraction/expansion parameters. R_l are radial Slater-type functions

$$R_l(r) = \frac{\xi_l^{nl+3}}{(n_l + 2)!} r^{nl} e^{-\xi_l r}.$$
(2)

The O, C and N atoms were refined up to octapolar level ($l_{\max} = 3$) and the H atoms up to dipole level ($l_{\max} = 1$). The n_l and ξ_l values were set equal to 2, 2, 2, 3 and 4.466 a.u.$^{-1}$ (O), 2, 2, 2, 3 and 3.176 a.u.$^{-1}$ (C), 2, 2, 2, 3 and 3.839 a.u.$^{-1}$ (N) and 1, 1 and 2.00 a.u.$^{-1}$ (H). The core and valence scattering factors were calculated from Clementi wavefunctions (Clementi & Roetti, 1974) and the anomalous dispersion was taken into account (Wilson, 1992). The refinement was performed for the reflections up to $s = 1.1$ Å^{-1}, with $I > 2\sigma(I)$ cut-off, which gives a satisfying number of reflections to parameter ratio greater than 15.

The atomic displacement parameters (ADPs) of H atoms were constrained to the values obtained from the SHADE server (Madsen, 2006) and H$-X$ distances were constrained to the values from neutron diffraction studies (Allen *et al.*, 2006). The ADPs and atomic positions of non-H atoms were then refined, first against all reflections [hereafter $s = 1.1$ Å^{-1}, with $I > 2\sigma(I)$] and then against high-order reflections ($s > 0.7$ Å^{-1}) using a spherical atom model, to ensure the deconvolution of the thermal motion from the deformation electron density (Hirshfeld, 1976).

Initially, the charge-density parameters of chemically equivalent atoms in the two molecules related by non-crystallographic symmetry were constrained to be the same. Local symmetry constraints were imposed (mirror planes for aromatic rings, nitro and amino groups, threefold axes for C atoms in methyl groups) to reduce the number of variables and to guarantee the physical meaningfulness of the refined
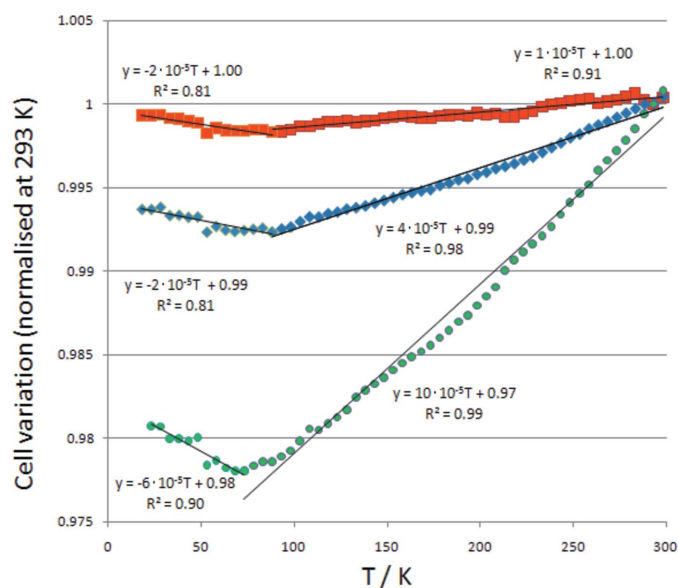

Figure 2
Cell-parameter variations in the powder diffraction experiment: $\Delta a/a$ – blue diamonds; $\Delta b/b$ – green dots; $\Delta c/c$ – red squares. This figure is in color in the electronic version of this paper.

parameters. κ and κ' parameters were set up to 1.16 and 1.0 for H and non-H atoms (Guillot, Viry *et al.*, 2001; Jelsch *et al.*, 2005).

Afterwards, the valence and multipole populations of all atoms and κ parameters of non-H atoms were refined against all reflections. The constraints were then gradually removed and all parameters were freely refined, excluding positions, ADPs and κ' coefficients of the H atoms, which were kept at the constrained values until the end of the refinement. In the last steps, the coordinates and the ADPs of all non-H atoms were refined alternatively with κ, valence and multipole populations for all atoms. The list of all multipole parameters is included in the CIF file.

The introduction of anharmonic nuclear motion for five atoms (N6, N6A, N8, O81 and O82; Kuhs, 1992; Sørensen *et al.*, 2003) was deemed necessary in order to take into account the high residual electron density around the N atoms of the amino group (N6, N6A), which could not be modeled properly even by splitting the N-atom positions, and to model the

electron density of one of the nitro groups (N8, O81, O82), which was found to be deformed in a similar manner as described recently (Zhurov *et al.*, 2011). These 0.37 (molecule 1) and 0.28 e Å^{-3} (molecule 2) peaks show up in the residual Fourier maps ($s < 0.9 \text{ Å}^{-1}$) in the planes bisecting the H61—N6—H62 moiety of both amino groups, at a distance of *ca* 0.5 Å from the N atoms. These Fourier residual peaks – which do not appear at a resolution of $s < 0.7 \text{ Å}^{-1}$ (*cf.* Figs. 3*a*–*c* harmonic model and Figs. 3*d*–*f* anharmonic model) – are a sign of disorder which can be modeled by third-order anharmonic motion. They cannot be interpreted as missing H atoms, because they appear when high-order reflections are included, while H atoms scatter at low $\sin\theta/\lambda$. The alternating occurrence of positive and negative residual density (nicknamed the 'shashlik' pattern) was already described as typical for non-modeled anharmonic nuclear motions of the third order (Meindl *et al.*, 2010; Herbst-Irmer *et al.*, 2010). The refined anharmonic coefficients are mostly not statistically significant, as shown in Table S3, but their use reduces the residual peak heights.
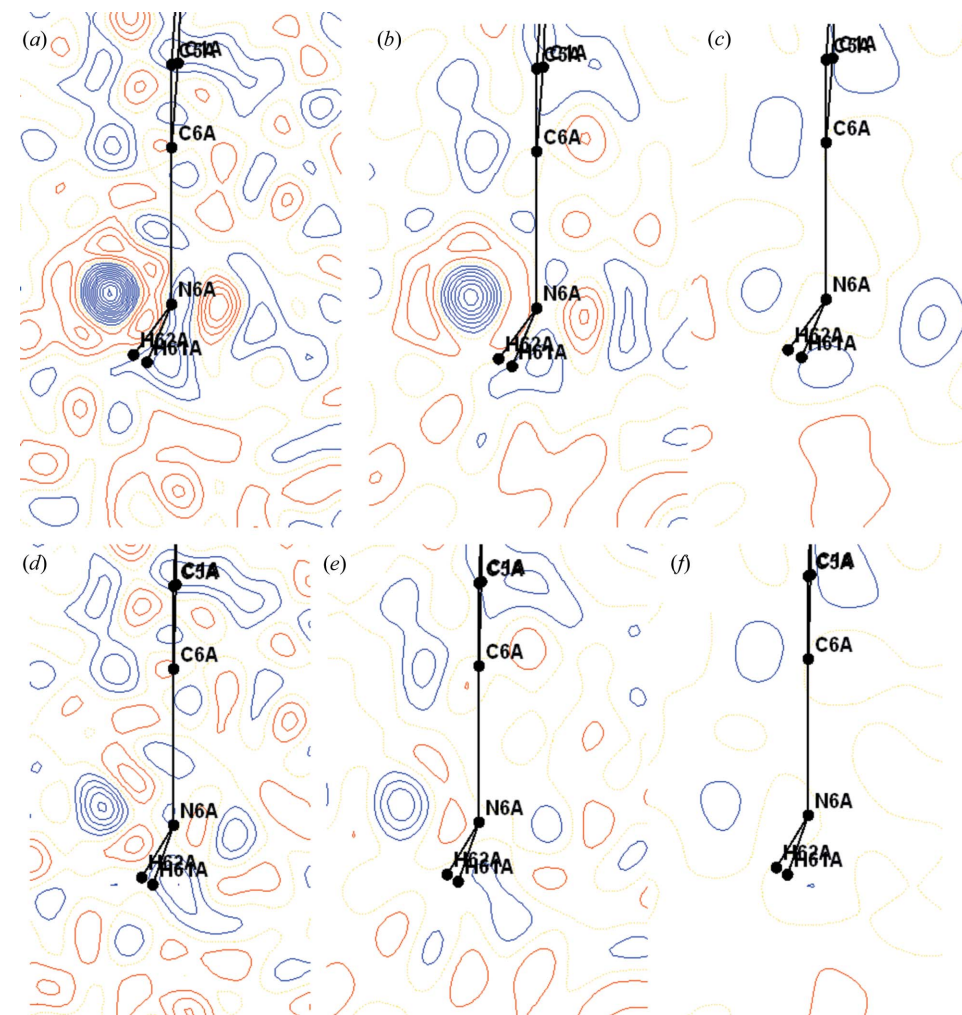
This refinement strategy is similar to that used by Zhurov *et al.* (2011) for hexahydro-1,3,5-trinitro-1,3,5-triazine. In both structures the introduction of anharmonicity significantly improved the modelling of the nitro groups. The reason why only one nitro group of the two chemically identical molecules is affected by anharmonic motion may be due to different surroundings in the crystal lattice. The nitro group refined with the harmonic model (N8*A*, O81*A*, O82*A*) is involved in a strong interaction with a neighboring amino group [O81*A*···H62*A*—N6*A*, $d(\text{O}\cdots\text{H}) = 2.026$ Å]. This restricts the vibration amplitudes, while for the second group refined with an anharmonic model (N8, O81, O82) the corresponding O82···H62—N6 distance is considerably larger [$d(\text{O}\cdots\text{H}) = 2.301$ Å].

To justify the necessity of refining all three atoms of the nitro group with an anharmonic model, the anharmonicity was gradually implemented into the model (first O81, second O82, third N8), and the resulting residual and static density maps were analyzed (Fig. 4). The optimal model, *i.e.* undistorted static deformation density and feature-

Figure 3
Residual electron-density maps after multipole refinement in the plane bisecting one of the NH$_2$ groups at different resolution for the model neglecting (*a*)–(*c*) and including (*d*)–(*f*) anharmonic nuclear motion; cut-off $I/\sigma I > 2$, contour 0.05 e Å^{-3}, blue – negative, red – positive. (*a*) and (*d*) $s < 1.1 \text{ Å}^{-1}$, (*b*) and (*e*) $s < 0.9 \text{ Å}^{-1}$, (*c*) and (*f*) $s < 0.7 \text{ Å}^{-1}$.

less residual density, was obtained after refining all three atoms in the anharmonic model.

The powder diffraction experiment was performed to relate anharmonicity with the possible occurrence of a phase transition. From 20 K to room temperature, the powder pattern was indexed in the same monoclinic cell. Fig. 2 depicts the temperature-dependent lattice parameters.

The biggest variation occurs for b. From room temperature to 75 K b decreases linearly with T ($\Delta b/b_{RT} = 10 \times 10^{-5}T + 0.97$) and suddenly increases for T smaller than 75 K ($\Delta b/b_{RT} = -6 \times 10^{-5}T + 0.98$). Similar but smaller changes occur for a, while c does not change significantly. These observations should be related to a structural phase transition; however, it was impossible to see growing $P2_1/c$ forbidden reflections with T, that would suggest lowering the symmetry to e.g. $P2_1$ or Pc space groups. As the space group of the crystal does not change, this observation may be related to an isostructural phase transition (see e.g. Bendeif et al., 2009) at ca 75 K. Further calorimetric measurements, as well as diffraction experiments below T_c, are needed to find out if it is anharmonicity or disorder.

This best multipole and anharmonic model was used in R_{free} calculations (Brünger, 1992, see §3) and it appeared that the best refinement is that with weak charge-density similarity restraints imposed on the two molecules. Therefore, the last steps of the refinement were repeated with the conditions proposed in §3.

The reliability of the U^{ij} parameters was confirmed by the low values of the Hirshfeld (1976) rigid-bond test (Table S1). There is only one bond (C7A–C71A) for which the value of ΔZ_{AB}^2 lies at the limit of acceptability, according to Hirshfeld (1976).

The residual electron-density maps for the final model ($R_1 = 0.030$, $S = 1.07$) in the main planes of the molecules show a randomly distributed electron density which generally does not exceed ± 0.10 e Å^{-3} (Fig. 5). The residual maps of the second molecule are available in the supplementary materials (Fig. S1).

3. Free R-factor calculations

The free R-factor calculations were performed to estimate if dissimilarities of the charge density between the two symmetry-independent molecules are reliable or due to noise and uncertainties. To the best of our knowledge this is one of the first attempts to use free R-factor calculations in the charge-density analysis of small organic molecules to find the level of optimal restraints. This method is still under testing, but we believe that the present
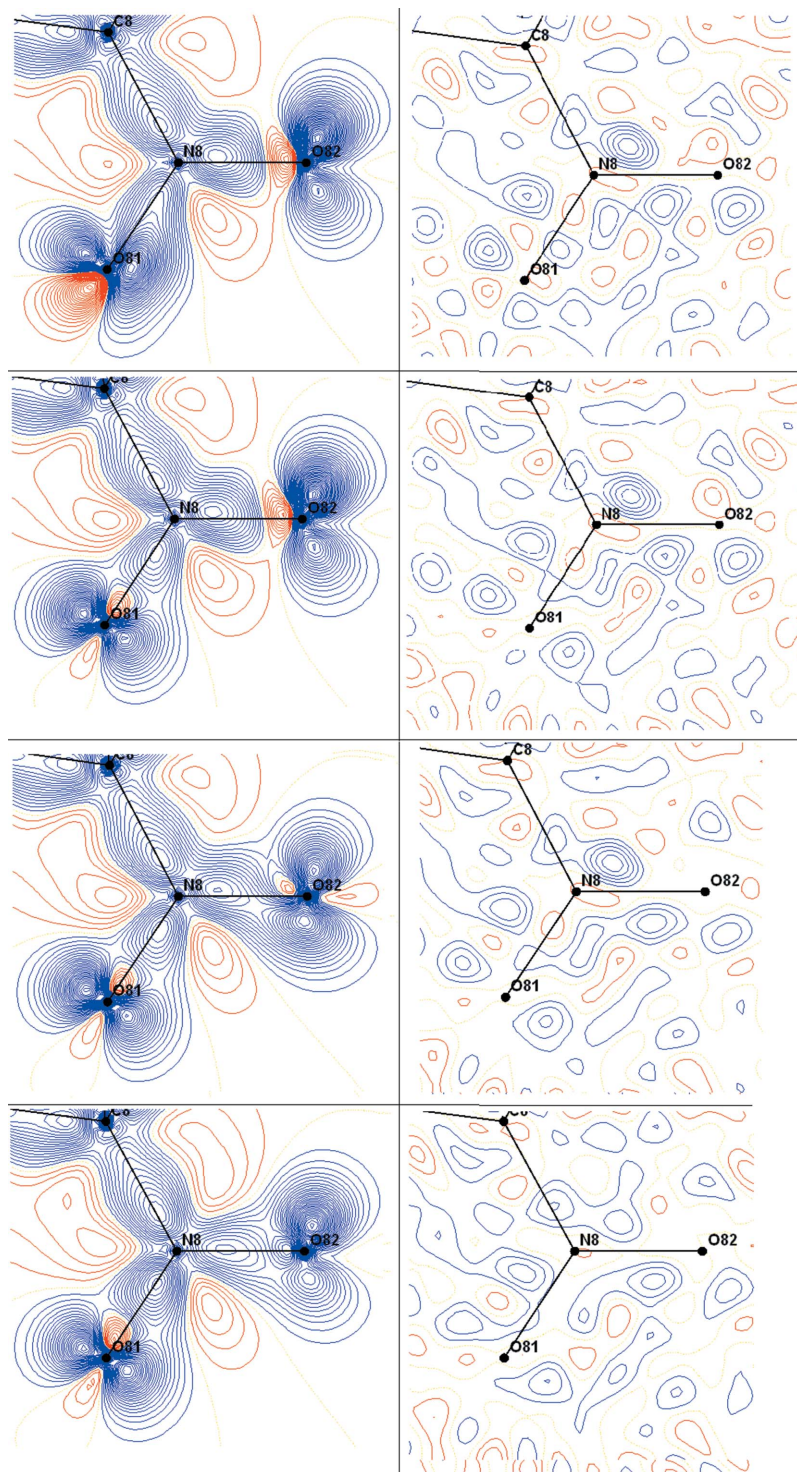

Figure 4
Static deformation (left) and residual (right) electron-density maps drawn in the plane of the NO₂ group in the harmonic model (1), with O81 treated as anharmonic (2), with both O atoms treated as anharmonic (3), and with the anharmonic model for all three atoms of the nitro group (4). Contours 0.05 e Å^{-3}, blue negative, red positive, $s < 1.1$ Å^{-1}.
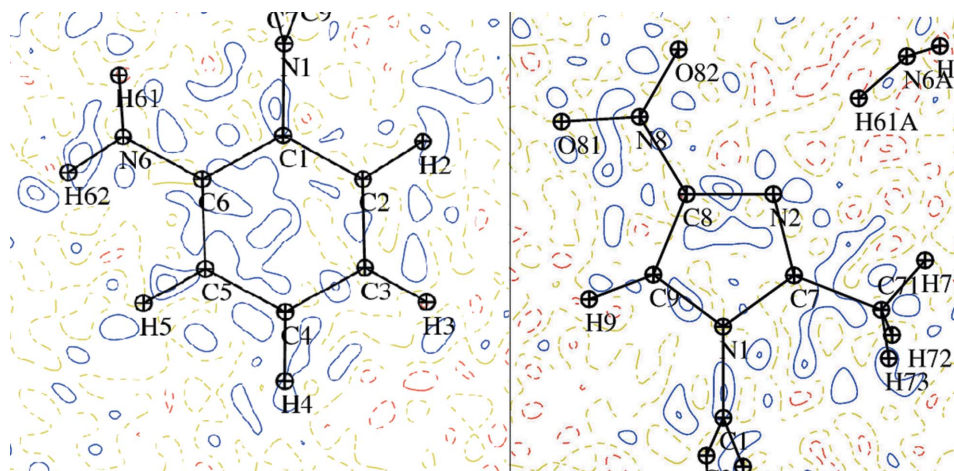
Figure 5
Residual electron-density maps for the phenyl ring plane (left) and nitroimidazole plane (right) of molecule (1); cut-off $I/\sigma I > 2$, resolution $s < 0.9$ Å^{-1}, contour 0.05 e Å^{-3}, blue – negative, red – positive.

calculations are valuable to bring us to reliable conclusions.

5% (1/20) of the reflections were used as a test set and the remaining 95% in the least-squares refinement. The free R factors were averaged over 20 individual free R factors obtained from 20 different refinements. Refinement strategies for free R calculations are proposed in the *MoPro* software (Jelsch *et al.*, 2005; Domagała & Jelsch, 2008). The refinement conditions were the following: resolution $s < 1.1$ Å^{-1}, $I > 2\sigma(I)$, the H-atom positions, ADPs and κ' were kept constrained, anharmonicity refined only at high order ($0.7 < s < 1.1$ Å^{-1}).
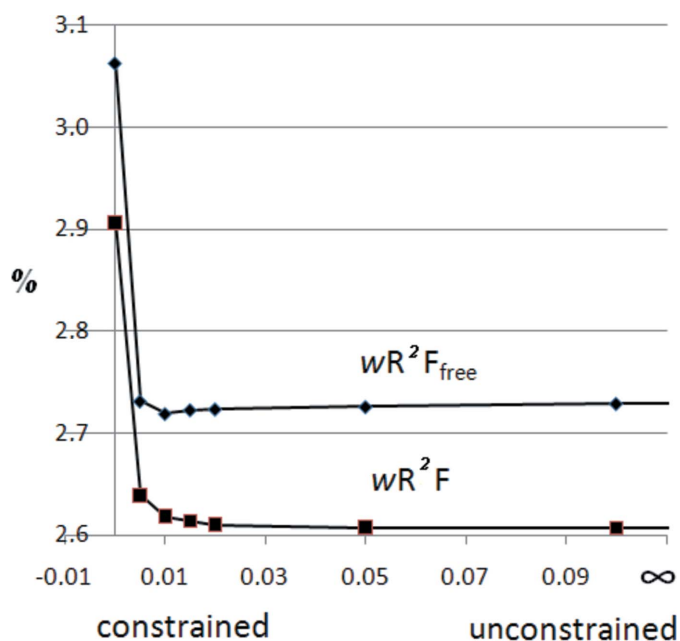

Figure 6
Crystallographic residual descriptors wR^2F and wR^2F_{free} as a function of σ_{Rsymul} for the first R-free series of tests.

Two series of refinement were performed, with a different level of restraints/constraints imposed. In the first series all κ coefficients, valence and multipole populations were constrained to be identical for the equivalent atoms in the two molecules. Varying restraint weights $w = 1/\sigma_r^2$ were applied to the symmetry of atoms ($\sigma_{\text{Rsymul}} = 0$; 0.005; 0.01; 0.015; 0.02; 0.05; 0.1; ∞). $\sigma_{\text{Rsymul}} = 0$ and ∞ refer to the constrained and unrestrained refinements. As expected and observed already (Domagała & Jelsch, 2008), the wR^2F factor decreases when weaker restraints are applied, and with regard to wR^2F_{free} there is a minimum ($wR^2F_{\text{free}} = 0.0272$) for moderately restrained refinement at $\sigma_{\text{Rsymul}} = 0.01$ (Fig. 6). The totally unconstrained refinement has a free R factor close to the minimum, while the constrained refinement yields higher free R-factor values.

Therefore, in the second series of calculations the symmetry restraints were fixed at the optimal value of $\sigma_{\text{Rsymul}} = 0.01$ and additional refinements were performed with varying levels of restraints imposed on valence and multipole populations and on the similarities of the κ values ($\sigma_{\text{Rsim}} = 0$; 0.02; 0.04; 0.05; 0.06; ∞). Trends similar to the previous refinement were observed for the two agreement factors plotted *versus* the level of restraints (Fig. 7). The minimum for the free R factor is reached at *ca* $\sigma_{\text{Rsim}} = 0.04$ with $wR^2F_{\text{free}} = 0.0267$), lower than the previous minimum of the first series of free R tests. This shows that the combination of the two types of restraints on the charge density yields a better refinement. The refinement with chemically equivalent atoms constrained to have the same charge-density parameters is not relevant for the current study as its wR^2F_{free} value is higher. However, the minimum value of wR^2F_{free} on Fig. 7 is less pronounced compared with Fig. 6. The wR^2F_{free} difference between the unconstrained and optimally restrained models is very small. This brings us to the conclusion that the quality of the diffraction data is high enough to allow the application of only weak charge-density similarity restraints and that the unconstrained refinement is not far from being optimal. Therefore, the charge-density distributions of the two molecules in the asymmetric unit can be compared with confidence.

3.1. Electron density computation

The deformation electron density is defined as the difference between the total molecular density described by the multipolar atom model and the superposition of spherical independent atoms (IAM – independent atom model). The experimental static deformation electron density was calcu-

Table 2
Distances and topological characteristics of the BCPs for the atoms involved in nitrogen groups in anharmonic (lines 1–8) and harmonic models (lines 9–16).

$D12$: distance between two atoms; $D1cp$, $D2cp$: distance from the first and the second atom to the critical point.

Atom 1	Atom 2	$D12$ (Å)	$D1cp$ (Å)	$D2cp$ (Å)	ρ_{tot} (e Å^{-3})	∇^2 (e Å^{-5})	λ_1 (e Å^{-5})	λ_2 (e Å^{-5})	λ_3 (e Å^{-5})	ϵ
C8	N8	1.4244 (4)	0.583	0.841	1.98	−15.2	−16.9	−13.2	14.9	0.22
C8A	N8A	1.4292 (4)	0.577	0.852	1.93	−14.1	−16.4	−12.8	15.1	0.22
N8	O81	1.2324 (4)	0.594	0.638	3.48	−11.2	−32.3	−30.3	51.4	0.06
N8A	O81A	1.2373 (4)	0.602	0.636	3.35	−7.7	−31.3	−28.3	51.8	0.09
N8	O82	1.2266 (4)	0.583	0.644	3.44	−12.0	−32.6	−30.1	50.7	0.07
N8A	O82A	1.2232 (3)	0.596	0.628	3.45	−8.2	−31.9	−28.5	52.2	0.11
C6	N6	1.3718 (4)	0.604	0.769	2.25	−16.7	−18.5	−15.7	17.6	0.15
C6A	N6A	1.3742 (4)	0.615	0.759	2.27	−17.5	−19.0	−15.7	17.2	0.17
C8	N8	1.4256 (4)	0.608	0.818	1.99	−14.1	−16.9	−13.5	16.3	0.20
C8A	N8A	1.4290 (4)	0.572	0.857	1.90	−13.7	−16.1	−12.3	14.7	0.23
N8	O81	1.2323 (4)	0.574	0.660	3.39	−8.4	−32.1	−29.2	52.8	0.09
N8A	O81A	1.2381 (4)	0.599	0.640	3.34	−6.1	−31.3	−28.2	53.4	0.10
N8	O82	1.2291 (4)	0.589	0.640	3.45	−10.5	−33.1	−30.2	52.8	0.09
N8A	O82A	1.2242 (3)	0.594	0.630	3.43	−6.2	−32.0	−28.6	54.4	0.11
C6	N6	1.3725 (4)	0.611	0.762	2.23	−15.2	−18.1	−15.3	18.2	0.15
C6A	N6A	1.3778 (4)	0.622	0.756	2.23	−15.9	−18.6	−14.8	17.5	0.21

lated from the crystallographic modeling as the atomic superposition sum over the molecule

$$\Delta\rho = \Sigma[P_{val}\kappa^3\rho_{val}(\kappa r) - N_{val}\rho_{val}(r) + \Sigma_l\kappa'3R_l(\kappa'r)\Sigma_m P_{lm\pm}(\theta, \emptyset)]. \quad (3)$$

The static and deformation maps were calculated using *VMoPro* and the plot with *MoProViewer* (Guillot, Viry *et al.*, 2001; Jelsch *et al.*, 2005; Guillot, 2010). The AIM charges and volumes were obtained with *WinxPro*, Version 1.548 (Stash & Tsirelson, 2002).

4. Results and discussion

4.1. Deformation electron density

The final model was obtained after refinement with the application of optimal similarity and symmetry restraints obtained after analysis of the wR^2F_{free} and wR^2F plots (Figs. 6 and 7). The static deformation-density maps (Figs. 8 and S2) drawn in the planes of the aromatic rings of both symmetry-independent molecules are qualitatively similar. Peaks of ∼ 0.7 e Å^{-3} are located in the middle of the aromatic C—C bonds. The densities between N1—C and N1A–C are polarized towards the N atoms in both molecules, as observed previously (Kubicki *et al.*, 2002). The multipole populations of the electron density of both amino groups are contracted in a similar manner to that reported for 5-nitro-2,4-dihydro-3*H*-1,2,4-triazol-3-one (Zhurova & Pinkerton, 2001).

In the nitroimidazole rings, the N-atom (N2, N2A) lone pairs are clearly visible, with the maximum density located in the plane of the ring, approximately 0.35 Å from the nitrogen nucleus position. This differs slightly from the distribution observed in 1-phenyl-4-nitroimidazole, where – in the absence of the C71 methyl group – the corresponding lone pair on the N atom reaches *ca* 0.5 e Å^{-3} and is situated 0.5 Å from the

nucleus position (Kubicki *et al.*, 2002). The bond polarization in the imidazole ring agrees with the results for imidazole, histidine and 1-phenyl-4-nitroimidazole (Ranganathan *et al.*, 2003; Liebschner *et al.*, 2009; Edwards, 1981).

The multipole representations of the deformation density of both nitro groups are similar and resemble that found in 1-phenyl-4-nitroimidazole (Kubicki *et al.*, 2002) and in the two explosive molecules RDX (hexahydro-1,3,5-trinitro-1,3,5-triazine) and HMX (octahydro-1,3,5,7-tetranitro-1,3,5,7-tetrazocine) (Zhurov *et al.*, 2011), with the interior lone pairs of the O atoms weaker than the exterior ones (*cf.* Figs. 4, 8 and S2).
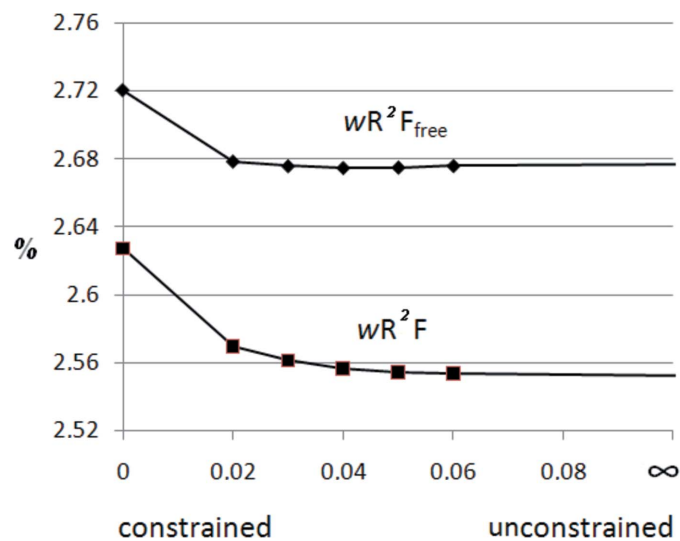

Figure 7
Crystallographic residual descriptors wR^2F and wR^2F_{free} as a function of σ_{Rsim} for the second series of the *R*-free tests. The multipole symmetry restraints were fixed at $\sigma_{Rsymul} = 0.01$.

Table 3
Atomic charges and volumes.

Molecule	$N_{val} - P_{val}$ (|e|)		AIM charge† (|e|)		Atomic volume† (Å³)		$N_{val} - P_{val}$ mol1–mol2	AIM charge mol1–mol2	V† mol1–mol2
	1	2	1	2	1	2			
C1	0.069	0.088	0.180	0.209	9.535	8.640	−0.019	−0.029	1.219
C2	−0.131	−0.123	−0.187	−0.203	14.247	11.685	−0.008	0.016	1.224
H2	0.092	0.098	0.153	0.152	7.393	6.042	−0.006	0.001	1.109
C3	−0.032	0.008	−0.064	0.088	12.483	11.257	−0.040	−0.152	0.913
H3	0.099	0.097	0.166	0.127	7.643	8.374	0.002	0.038	0.900
C4	−0.013	−0.002	−0.061	−0.087	10.858	12.070	−0.011	0.026	0.961
H4	0.095	0.114	0.111	0.129	6.450	6.710	−0.019	−0.017	0.999
C5	0.018	−0.013	0.020	0.027	12.373	12.381	0.031	−0.007	1.213
H5	0.120	0.110	0.149	0.131	8.901	7.335	0.010	0.018	0.998
C6	0.001	0.007	0.245	0.283	8.746	8.767	−0.006	−0.038	0.897
N6	−0.405	−0.424	−1.217	−1.200	18.314	20.410	0.019	−0.018	0.910
H61	0.307	0.297	0.553	0.526	2.539	2.791	0.010	0.027	1.051
H62	0.255	0.281	0.538	0.514	3.088	2.937	−0.026	0.024	1.014
N1	−0.350	−0.305	−0.974	−0.933	10.702	10.558	−0.045	−0.041	0.926
C9	−0.002	0.013	0.150	0.177	11.573	12.501	−0.015	−0.027	1.177
H9	0.170	0.173	0.250	0.246	6.719	5.708	−0.003	0.004	0.840
C8	0.074	0.087	0.482	0.486	7.245	8.622	−0.013	−0.004	0.937
N8	−0.043	−0.086	0.296	0.237	7.221	7.710	0.043	0.059	1.051
O81	−0.255	−0.264	−0.505	−0.458	19.427	18.477	0.009	−0.048	0.921
O82	−0.298	−0.301	−0.537	−0.539	18.249	19.821	0.003	0.003	1.047
N2	−0.187	−0.219	−0.736	−0.814	14.310	13.663	0.032	0.078	1.005
C7	0.106	0.168	0.650	0.705	7.341	7.301	−0.062	−0.055	1.257
H71	0.160	0.205	0.172	0.273	7.643	6.081	−0.045	−0.101	1.041
H72	0.145	0.130	0.177	0.180	6.896	6.626	0.015	−0.003	0.958
H73	0.137	0.154	0.163	0.170	5.738	5.987	−0.017	−0.007	0.901
C71	−0.204	−0.224	−0.242	−0.345	10.907	12.104	0.020	0.103	1.219
Sum	−0.070	0.070	−0.069	0.080	256.540	254.559			

† Integrated atomic charges and volumes (Stash & Tsirelson, 2002).

4.2. Topological analysis of covalent bonds

Selected bond-critical points for both harmonic and anharmonic models are listed in Table 2 (the full list is in Table S5) and depicted in Fig. S3.

The bond-critical points of the atoms refined in anharmonic/harmonic models do not differ in terms of distances to the two involved atoms. ADPs of these five anharmonic atoms in the two models are equal within 3σ. However, some variations are observed for Laplacian and electron density values – in general, the anharmonic model increases the Laplacian value.

The C—C $(3,-1)$ critical points of the phenyl rings [⟨C—C⟩ = 1.397 (8) Å, with the longest bonds C1—C6 and C5—C6 of the two molecules in the range 1.403–1.410 Å, cf. Table S5] are in the centre of these bonds [⟨C—CP⟩ = 0.698 (20) Å] and the total electron density values at these points are nearly identical ⟨2.16 (5) e Å^{-3}⟩, with the exception of C5—C6 bonds (ρ_{tot} = 2.06 and 2.05 e Å^{-3}, in both symmetry-independent molecules), where the densities are slightly depleted, probably due to the vicinity of the NH$_2$ groups. The influence of the electronegative N atoms is more pronounced in the C—N bonds, where the CPs are clearly moved towards the C atoms, in relation to the larger atomic basin of the N atoms (Kubicki et al., 2002).
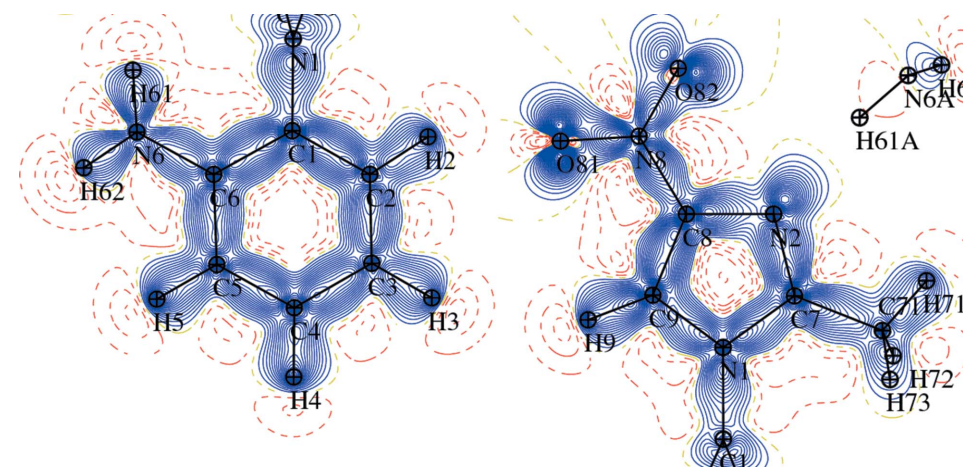
The biggest differences between the two symmetry-independent molecules of (1) concern the Laplacian $\nabla^2\rho$ at the critical points connected with the N=O bonds (cf. Table 2), but the results lie within the range found in the literature. For the first molecule, the $\nabla^2\rho$ values for these bonds are

Figure 8
Deformation density maps drawn in the planes of imidazole (left) and phenyl (right) rings, contour 0.05 e Å^{-3}, blue – negative, red – positive.

Table 4
Distances (Å) and angles (°) in the hydrogen bonds.

$D-H\cdots A$	$D-H$	$H\cdots A$	$D\cdots A$	$D-H\cdots A$
N6A—H62A···O81A[i]	1.009	2.026	3.0324 (4)	174.9
N6—H61···N2A	1.009	2.150	3.0747 (4)	151.6
N6A—H61A···N2	1.009	2.196	3.1654 (4)	160.5
N6—H62···O82[ii]	1.009	2.301	3.2095 (4)	149.1
C71—H72···O82[i]	1.059	2.551	3.1339 (4)	113.9
C4A—H4A···O81[iii]	1.083	2.367	3.1776 (4)	130.4
C4A—H4A···O81A[iii]	1.083	2.507	3.3996 (4)	139.0
C2A—H2A···N2A[iv]	1.083	2.440	3.4526 (4)	155.1
C9A—H9A···N2[v]	1.083	2.460	3.4522 (3)	151.8
C4—H4···C4A[vi]	1.083	2.624†	3.6586 (4)	159.8
C71A—H73A···C5[vi]	1.059	2.819†	3.8117 (5)	156.0

Symmetry codes: (i) $-x+1, y-\frac{1}{2}, -z+\frac{1}{2}$; (ii) $-x+1, -y+1, -z$; (iii) $x+1, y, z$; (iv) $-x+1, -y+2, -z$; (v) $-x+1, y+\frac{1}{2}, -z+\frac{1}{2}$; (vi) $x, -y+\frac{1}{2}, -z-\frac{3}{2}$. † Distance to the closest atom in the aromatic ring.

close to those found in another currently investigated nitroimidazole derivative, 2-methyl-4-nitro-1-phenyl-1H-imidazole-5-carbonitrile (Paul, 2011). The Laplacian values for the second molecule are closer to those reported for 1-phenyl-1,4-nitroimidazole and 5-nitro-2,4-dihydro-3H-1,2,4-triazol-3-one (Kubicki *et al.*, 2002; Zhurova & Pinkerton, 2001). These double N=O bonds present the highest electron-density concentration and therefore the estimation of their second derivatives and of the positions of the critical points is not straightforward. These values are the derivatives of the experimental electron density, therefore, the subtle changes of ρ_{tot} bring much higher differences in the critical point position and Laplacian values.

4.3. Atomic charges and volumes

The comparison and discussion of atomic charges is usually difficult because of the different definitions (Koritsanszky & Coppens, 2001). In the case of (1), with two chemically equivalent molecules in the asymmetric unit and therefore expected similar characteristics, the comparison might be more reasonable. The comparison was performed based on the monopole valence derived charges $N_{val}-P_{val}$ and on the integrated atomic charges (Stash & Tsirelson, 2002). Some variations may be expected due to different intermolecular interactions.

The two symmetry non-equivalent molecules have nearly the same atomic charge values for a chosen charge definition (Table 3). The charge values and, in some cases, even the signs for individual atoms and functional groups (*e.g.* amino or nitro) depend on the definition. For instance, the monopole P_{val}-derived charges of the amino groups are positive (0.157 and 0.154 |e|), but the integrated values are negative (-0.126 and -0.116 |e|). For the nitro groups, the differences are larger and, in all cases, the charge is negative (multipolar: -0.566 and -0.746 |e|; integrated: -0.746 and -0.760 |e|). Similar behavior was observed for the charges of another nitroimidazole derivative (Kubicki *et al.*, 2002), where the nitro group charges were equal to -0.34 (multipolar) and -0.62 |e| (integrated).

The P_{val} derived atomic charges show a correlation coefficient of $r = 99.16\%$ between the two molecules, while for the AIM charges it is even higher at $r = 99.37\%$. The root mean-square deviation of the P_{val} and AIM charges is 0.025 and 0.051 |e|. This is slightly larger than the average uncertainty of the P_{val} parameters which is ~ 0.017 |e|.

The imidazole N atoms (N1, N1A, N2, N2A) display an electron-withdrawing effect on the neighboring C atoms, which is especially evident in the integrated charge values, as was also noticed before (Kubicki *et al.*, 2002). This general trend agrees with the static deformation density maps (Figs. 4, 8 and S2).

5. Hydrogen bonds

5.1. Geometrical criteria

In molecule (1) there are two strong hydrogen-bond donors (NH$_2$ groups), one strong acceptor (imidazole N2 atoms), two significantly weaker acceptors (O atoms from nitro groups) and a number of weak donors (C—H) and acceptors (π-systems). As expected, the best donors interact with the best acceptors leading to strong N—H···N and N—H···O hydrogen bonds (*cf.* Table 4). These strong hydrogen bonds link the symmetry-independent molecules into a dimer, which can be regarded as the building block of the structure. The mutual packing of these dimers is then determined by weak but directional C—H···O, C—H···N and C—H···π interactions; more geometrical details of the crystal packing can be found in Kubicki & Wagner (2008).

5.2. Topological analysis

The existence and strength of the hydrogen bonds can be analyzed by means of criteria proposed by Koch & Popelier (1995), based on the AIM theory (Bader, 1990). According to this approach, to recognize a H···A interaction as a hydrogen bond the following conditions have to be met:

(i) the bond-critical point (BCP) must be found between H and A atoms,

(ii) the value of the electron density ρ at the BCP has to be correlated with the bond energy,

(iii) the Laplacian $\nabla^2\rho$ at the BCP must have a positive value, and

(iv) there is a mutual penetration of H and A atoms.

According to Koch and Popelier, these first four out of a total of eight conditions are necessary and sufficient to recognize an interaction as a hydrogen bond.

In the structure of (1), the $(3,-1)$ critical points and the corresponding bond paths were found for the strongest 11 interactions (Table 4), but also for 16 additional C—H···O, C—H···N, C—H···C$_{ar}$ and H···H contacts (see Table 5). The intermolecular critical points found between aromatic rings will not be discussed here, as the total density values at the CPs are very low and the eigenvectors values lie at the limit of acceptability for the $(3,-1)$ type of critical points.

The total energy density and the positive Laplacian $\nabla^2\rho$ values at the CPs were plotted *versus* the electron density ρ_{cp}

Table 5
Topological characteristics of the intermolecular interactions.

cp	Atom 1	Atom 2	$D12$ (Å)	$D1cp$ (Å)	$D2cp$ (Å)	ρ_{tot} (e Å^{-3})	$\nabla^2\rho$ (e Å^{-5})	λ_1 (e Å^{-5})	λ_2 (e Å^{-5})	λ_3 (e Å^{-5})	ϵ	$G(\mathbf{r}_{CP})$ (kJ mol^{-1} a.u.$^{-3}$)	$V(\mathbf{r}_{CP})$ (kJ mol^{-1} a.u.$^{-3}$)	$H(\mathbf{r}_{CP})$ (kJ mol^{-1} a.u.$^{-3}$)
Strong hydrogen bonds: N—H···O and N—H···N														
cp1	N6A—H62A	O81A^{i}	2.0261	0.715	1.314	0.060	2.47	−0.25	−0.24	2.96	0.04	47.8	−28.1	19.7
cp2	N6—H61	N2A	2.1496	0.809	1.393	0.069	1.69	−0.34	−0.26	2.30	0.25	34.3	−22.6	11.7
cp3	N6A—H61A	N2	2.1962	0.790	1.437	0.060	1.67	−0.27	−0.22	2.29	0.07	33.2	−21.0	11.2
cp4	N6—H62	O82^{ii}	2.3014	0.924	1.436	0.046	1.07	−0.21	−0.17	1.44	0.18	21.2	−13.4	7.8
Moderate strength hydrogen bonds: C—H···O, C—H···N														
cp5	C2A—H2A	N2A^{iii}	2.4400	0.958	1.507	0.046	0.94	−0.17	−0.16	1.26	0.04	18.9	−12.2	6.7
cp6	C4A—H4A	O81^{iv}	2.3671	1.001	1.396	0.058	1.05	−0.25	−0.21	1.50	0.15	21.7	−15.0	6.7
cp7	C9A—H9A	N2^{v}	2.4597	0.958	1.543	0.038	0.86	−0.16	−0.12	1.13	0.24	16.9	−10.5	6.4
cp8	C4A—H4A	O81A^{iv}	2.5068	1.055	1.490	0.036	0.74	−0.15	−0.11	1.00	0.26	14.6	−9.2	5.4
cp9	(C71—H72)^{v}	O82	2.5514	1.208	1.414	0.059	0.85	−0.21	−0.12	1.18	0.43	18.3	−13.4	4.9
Hydrogen bonds with π acceptors: C—H···C$_{ar}$														
cp10	(C4—H4)^{ii}	C4A	2.6235	1.034	1.659	0.040	0.66	−0.11	−0.04	0.81	0.64	13.4	−8.8	4.6
cp11	(C71A—H73A)^{ii}	C4	2.8915	1.188	1.723	0.033	0.44	−0.09	−0.03	0.56	0.63	9.0	−6.1	2.9
Weak interactions: C—H···O, C—H···N, C—H···C														
cp12	C3—H3	O82A^{vi}	2.7174	1.110	1.620	0.026	0.44	−0.08	−0.06	0.59	0.23	8.7	−5.4	3.3
cp13	C71A—H71A	N6	2.8747	1.200	1.737	0.025	0.40	−0.08	−0.05	0.52	0.41	7.9	−4.9	3.0
cp14	C2A—H2A	N6^{iii}	2.9352	1.276	1.746	0.026	0.39	−0.08	−0.05	0.52	0.32	7.8	−5.0	2.8
cp15	C71A—H73A	C71	3.1404	1.386	1.842	0.030	0.39	−0.10	−0.03	0.51	0.73	8.0	−5.4	2.6
cp16	C3A—H3A	O82A^{iv}	3.0250	1.449	1.641	0.020	0.33	−0.05	−0.05	0.43	0.15	6.5	−4.0	2.5
cp17	C2—H2	O81A^{vi}	2.9445	1.375	1.628	0.021	0.32	−0.06	−0.05	0.43	0.09	6.3	−3.9	2.4
cp18	C3—H3	O82A^{vii}	2.9909	1.375	1.671	0.016	0.26	−0.05	−0.04	0.35	0.08	5.0	−3.0	2.0
cp19	(C71—H71)^{ii}	N6	3.3152	1.459	1.862	0.015	0.24	−0.04	−0.01	0.30	0.65	4.7	−2.8	1.9
cp20	C71—H72	N6A^{v}	3.2454	1.443	1.884	0.015	0.22	−0.04	−0.01	0.27	0.67	4.3	−2.6	1.7
cp21	C5—H5	O81^{ii}	2.9852	1.321	1.761	0.009	0.21	−0.03	−0.02	0.26	0.31	3.9	−2.2	1.7
cp22	C4—H4	O82A^{vii}	3.1788	1.501	1.733	0.013	0.20	−0.03	−0.02	0.25	0.43	3.9	−2.3	1.6
H···H contacts														
cp23	C2—H2	(H5A—C5A)^{v}	2.0989	0.973	1.199	0.036	0.75	−0.12	−0.12	0.99	0.02	14.8	−9.3	5.4
cp24	C4—H4	(H9—C9)^{vii}	2.2576	1.337	1.008	0.035	0.66	−0.13	−0.10	0.89	0.28	13.2	−8.4	4.8
cp25	C71—H73	(H73—C71)^{ii}	2.1638	1.082	1.082	0.035	0.62	−0.13	−0.11	0.86	0.13	12.4	−7.9	4.5
cp26	C71—H72	(H71A—C71A)^{ii}	2.3262	1.302	1.143	0.040	0.52	−0.15	−0.07	0.74	0.55	11.0	−7.7	3.3
cp27	N62—H62A	(H9A—C9A)^{i}	2.4484	1.248	1.223	0.023	0.42	−0.09	−0.07	0.57	0.23	8.1	−5.0	3.1

Symmetry codes: (i) $-x + 1, y - \frac{1}{2}, -z + \frac{1}{2}$; (ii) $-x + 1, -y + 1, -z$; (iii) $-x + 1, -y + 2, -z$; (iv) $x + 1, y, z$; (v) $-x + 1, y + \frac{1}{2}, -z + \frac{1}{2}$; (vi) $x, y - 1, z$; (vii) $-x, -y + 1, -z$.

for all intermolecular contacts except H···H. These properties are linear *versus* the interatomic distances (*cf.* Fig. S4), as shown by Espinosa *et al.* (1999). The fourth criterion concerning the mutual penetration of the H and acceptor
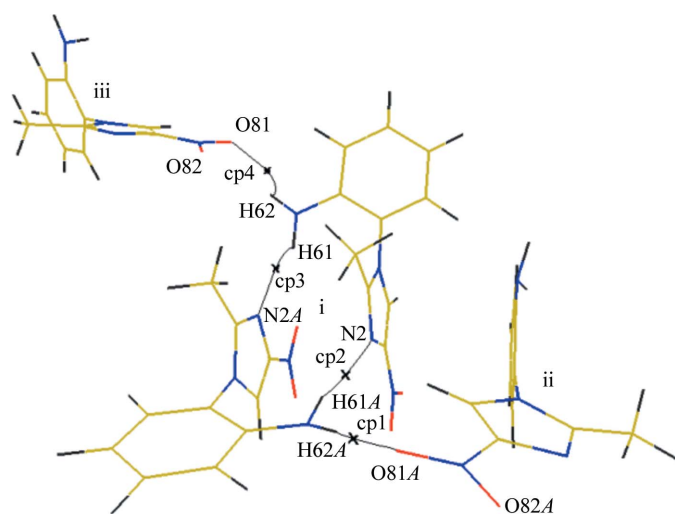

Figure 9
Critical points found along the strongest hydrogen interactions. Symmetry codes: (i) x, y, z; (ii) $-x + 1, y - \frac{1}{2}, -z + \frac{1}{2}$; (iii) $x, -y + \frac{3}{2}, z - \frac{1}{2}$.

atoms can be estimated using van der Waals (vdW) atomic radii (Bondi, 1964; Mantina *et al.*, 2009; 1.1 Å for H, 1.52 Å for O, 1.55 Å for N and 1.70 Å for C). However, one should keep in mind that the vdW radii themselves are rather a fuzzy concept and what is more, they differ depending on the theoretical methods or experimental structural data used. To estimate the penetration of the H and acceptor atoms, the non-bonded radii have to be compared with bonded radii. Within the AIM theory, the bonded radii are the distances from the H and acceptors atoms to the appropriate critical points (Koch & Popelier, 1995). The sum $\Delta r_{\rm H} + \Delta r_A$ has to be positive to fulfill the conditions for hydrogen bonds (*cf.* Table 6). Due to the ambiguity on the definition of vdW radii, the H73A···C4$_\pi$ interaction (cp11), for which this sum has a small negative value, is considered to be borderline.

The four strongest hydrogen bonds, for which critical-point positions are depicted in Fig. 9, are associated with the highest values of ρ_{cp} and the Laplacian, which vary from 0.046 to 0.069 e Å^{-3} and 1.07 to 2.47 e Å^{-5}. These values are in agreement with the literature data for moderate strength interactions (Espinosa *et al.*, 1999; Ranganathan *et al.*, 2003; Hoser *et al.*, 2009).

The following interactions (involving cp5 to cp9) are all classified as weak hydrogen bonds. They are still clearly distinguishable from the remaining contacts, with ρ_{cp} in the

Table 6
Mutual penetrations (Å) of the hydrogen-acceptor atoms.

	Δr_H	Δr_A	$\Delta r_H + \Delta r_A$		Δr_H	Δr_A	$\Delta r_H + \Delta r_A$
cp1	0.385	0.206	0.591	cp12	−0.100	−0.099	−0.199
cp2	0.291	0.157	0.448	cp13	−0.100	−0.187	−0.287
cp3	0.310	0.113	0.423	cp14	−0.176	−0.196	−0.372
cp4	0.176	0.084	0.260	cp15	−0.286	0.142	−0.429
cp5	0.142	0.043	0.185	cp16	−0.349	−0.121	−0.470
cp6	0.099	0.124	0.223	cp17	−0.275	−0.108	−0.383
cp7	0.142	0.007	0.149	cp18	−0.275	−0.151	−0.426
cp8	0.045	0.030	0.075	cp19	−0.359	−0.312	−0.671
cp9	−0.108	0.106	−0.003	cp20	−0.343	−0.334	−0.677
cp10	0.066	0.041	0.107	cp21	−0.221	−0.241	−0.461
cp11	−0.088	−0.023	−0.111	cp22	−0.401	−0.213	−0.614

Δr_H and Δr_A are the differences between the vdW radii and bonded radii for the hydrogen and acceptor atom, respectively.

range 0.036–0.059 e Å^{-3} and Laplacian values between 0.74 and 1.05 e Å^{-5}, which are close to those reported before (*e.g.* Guillot *et al.*, 2008; Kubicki *et al.*, 2002). The next two C—H⋯C_{ar} contacts (cp10–11) lie at the limit of the Koch &

Popelier (1995) criteria, at the borderline between hydrogen bonds and vdW interactions, as indicated by the negative sign of the sum $\Delta r_H + \Delta r_A$ (cp11). Most stabilizing C—H⋯π interactions are directional, with C—H⋯C_{ar} (the closest C atom in the phenyl ring) angles of 156.0 and 159.8°, but the distances between H atoms and the six C atoms of the aromatic rings lie between 2.75–3.55 and 2.58–3.51 Å, much longer than observed in the literature (Madhavi *et al.*, 1997, references therein). This can be taken as further proof that they are at the very limit of hydrogen bonds.

For comparison, we performed the same calculations with crystal data for the drug Fidarestat (Fournier *et al.*, 2009). The strong and weak hydrogen bonds were analyzed for all eight interactions, including some with aromatic rings as acceptors; in all cases the sum of $\Delta r_H + \Delta r_A$ had positive values. Beside the primary and secondary interactions, additional C—H⋯O, C—H⋯N and C—H⋯C contacts, with CPs and bond paths, were found for (1) (cp12–cp22). Aromatic or methyl C—H groups act as hydrogen-bond donors and N, O or (aromatic) C atoms act as acceptors in these contacts.

The list of possible intermolecular interactions is closed by hydrogen–hydrogen contacts. The H atoms which are involved in these potential interactions all have very similar charges; therefore, it is not 'dihydrogen bonding' but 'hydrogen–hydrogen bonding' (Hernández-Trujillo & Matta, 2007; Matta *et al.*, 2003; Grabowski, 2006). It is therefore interesting to map the topological properties of these contacts and compare them to the stronger interactions. The gradient vector maps of the static electron density depicted in Fig. 10 and S5 clearly show the existence of the (3,−1) critical points.

Comparison of the two molecules in terms of the number of intermolecular contacts allows us to conclude that for the stronger interactions (cp1–11), molecule *A* is more often involved as a H-atom donor (seven times) than as an acceptor (five times), whereas *B* is more involved in weaker interactions (cp 12–22). The hydrogen–hydrogen contacts are mostly formed by the first molecule.

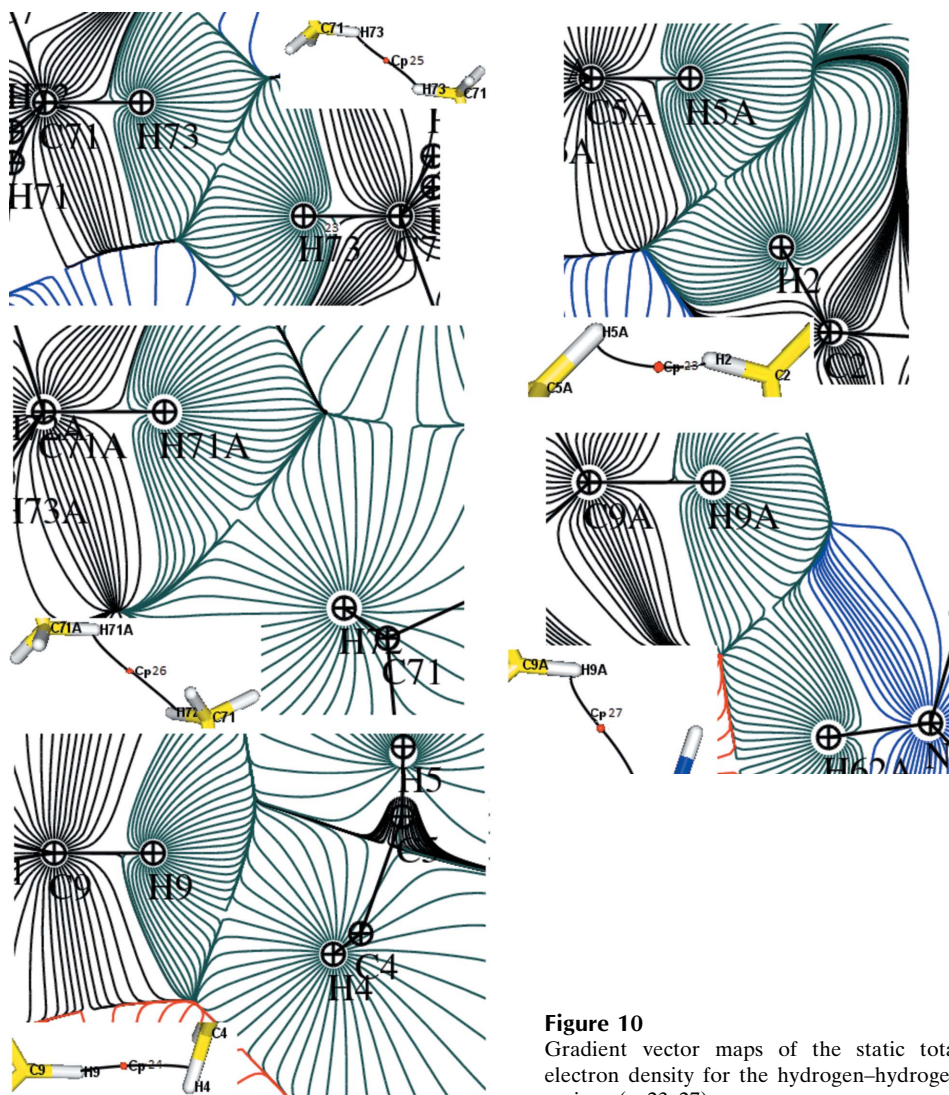Figs. 11 and 12 depict the relation between the Laplacian and the

Figure 10
Gradient vector maps of the static total electron density for the hydrogen–hydrogen regions (cp23–27).

λ_3 eigenvalue (along the direction of the interaction pathway) at the CPs and the intermolecular distance [for a similar plot of $\rho_{tot}(d_{H \cdots A})$ see Fig. S6]. A linear dependence is found for

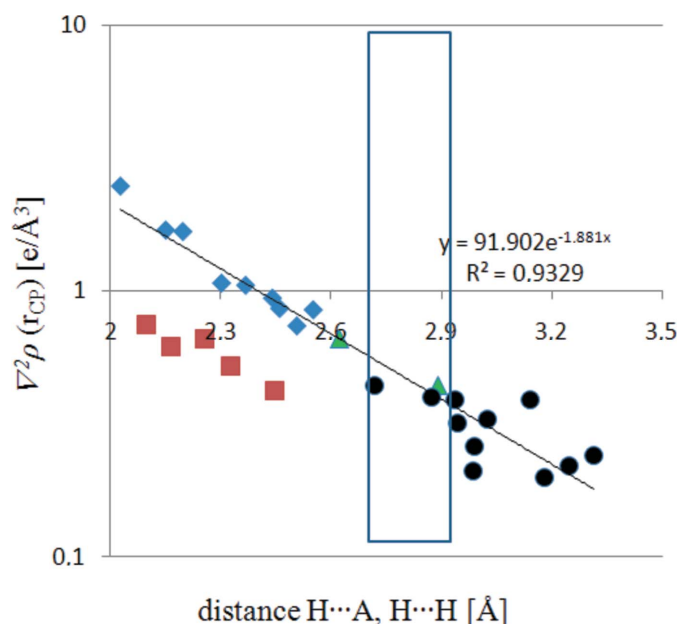**Figure 11**
Linear dependence of the Laplacian $\nabla^2 \rho$ at the CP (in logarithmic scale) on the $H \cdots A$ distance. The blue diamonds (cp1–9) represent strong hydrogen bonds, the green triangles (cp10–11) hydrogen bonds with a π acceptor, black dots (cp 12–22) weak interactions. The rectangle shows the region of overlap between hydrogen bonds and van der Waals interactions. H—H contacts (cp23–27, red squares) are not included in the exponential fitting. This figure is in color in the electronic version of this paper.
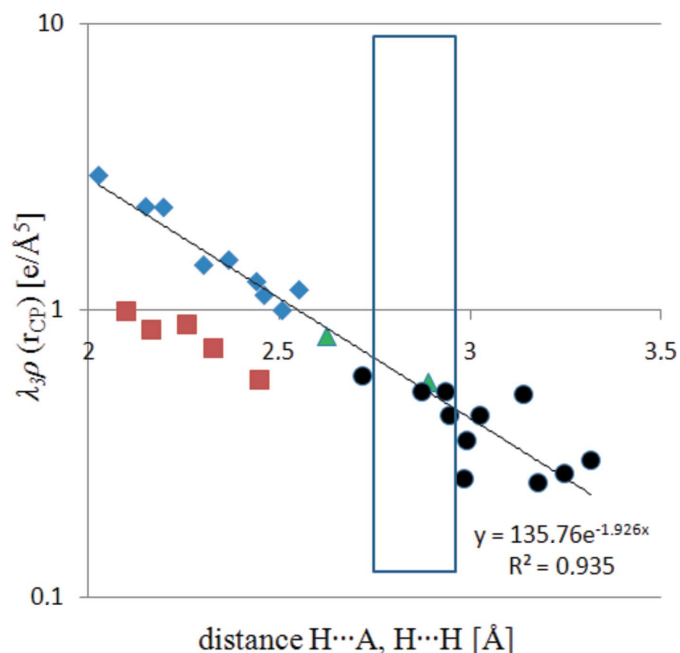
Figure 12
Linear dependence between the positive Hessian curvature (in logarithmic scale) and the $H \cdots A$ distance. The CP symbols are the same as in Fig. 11. This figure is in color in the electronic version of this paper.

both properties, even for $H \cdots H$ contacts. The $C—H \cdots C_{ar}$ contacts, as described before, are located at the limit between hydrogen bonds and van der Waals interactions. A similar overlapping region was presented in previous experimental and theoretical studies for substituted coumarins (Munshi & Row, 2005a,b).

The following plots highlight the exponential relations between the kinetic and potential energy densities (calculated from Abramov's equation; Abramov, 1997) and the interatomic distance (Fig. 13) and the linear dependence of the total energy density $[V(\mathbf{r}_{CP}) + G(r_{CP})]$ on the positive Hessian curvature (Fig. 14).

These simple empirical relations between energetic and topological characteristics were previously found to be valid for a wide range of hydrogen-bond interactions (Espinosa et al., 1999; Ranganathan et al., 2003; Hoser et al., 2009) and have been questioned owing to their simplicity (Koritsanszky, 2006, and references therein). They also appear here for closed-shell van der Waals interactions and $H \cdots H$ 'bonds', and the data reported here might be regarded as further proof of their validity.

6. Conclusions

The charge-density distribution in crystals of 1-(2′-aminophenyl)-2-methyl-4-nitroimidazole has been experimentally determined by means of high-resolution X-ray diffraction. Anharmonicity modeling has been successfully used to reduce residual electron density on some N atoms of amino groups and one of the nitro groups, which improved the model and the picture of the static deformation and residual densities.

The R_{free} calculations revealed that the optimal model is a model with weak, partial similarity restraints on the expansion/contraction coefficients and valence/multipole popula-
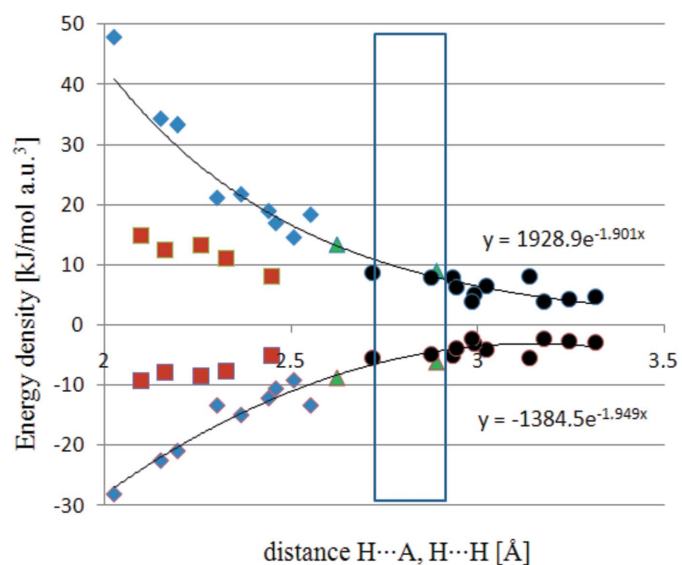

Figure 13
The exponential dependence of the potential (negative side) and kinetic (positive side) energy density on the $H \cdots A$ distance. The CP symbols are the same as in Fig. 11. This figure is in color in the electronic version of this paper.

Figure 14
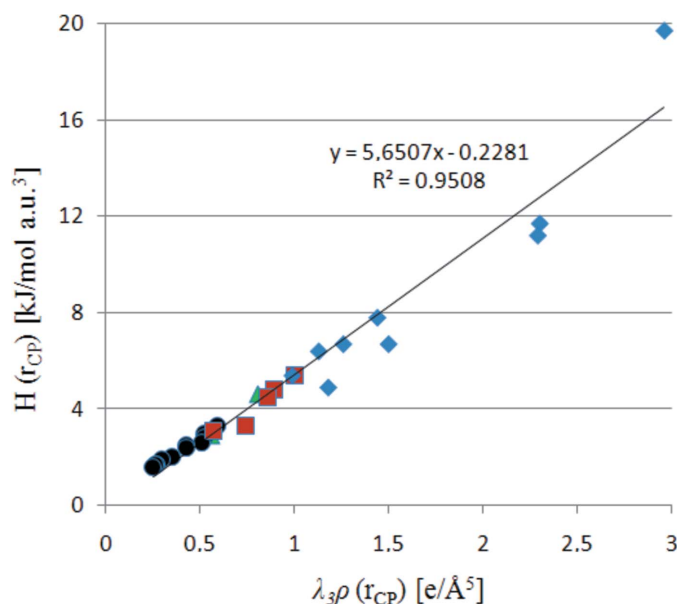Linear dependence between the total energy density $H(\mathbf{r}_{cp})$ and the λ_3 eigenvalue at the CPs. The CP symbols are the same as in the Fig. 11. This figure is in color in the electronic version of this paper.

tions between the two molecules of (1). The anharmonicity applied to only one of the two nitro groups, beside the common amino group treatment, is the greatest difference between the two molecules in the crystal structure.

The topological analysis using the AIM approach was performed in order to assess the influence of additional functional groups on the resulting interactions and the differences between two different molecules in the asymmetric unit. Beside the stronger hydrogen bonds and $C-H\cdots C_{ar}$ interactions, other interactions were found in the range between weak hydrogen bonds and van der Waals interactions. Additional $H\cdots H$ contacts were also found, which can be regarded as hydrogen–hydrogen interactions. These unpredicted stabilizing contacts successfully supplement the van der Waals interactions, as for all investigated parameters (Figs. 11–13), the concerned CPs are located in the region of weak hydrogen bonds.

The charge-density distribution obtained in the course of this study is in good agreement with the previously published structure of 1-phenyl-4-nitroimidazole (Kubicki *et al.*, 2002), with some deviations that can be attributed to the different substituent groups.

References

Abramov, Yu. A. (1997). *Acta Cryst.* A**53**, 264–272.
Allen, F. H., Watson, D. G., Brammer, L., Orpen, A. G. & Taylor, R. (2006). *International Tables for Crystallography*, Vol. C, 1st online ed., ch. 9.5, pp. 790–811. Chester: International Union of Crystallography.
Altomare, A., Cascarano, G., Giacovazzo, C. & Guagliardi, A. (1993). *J. Appl. Cryst.* **26**, 343–350.
Bader, R. F. W. (1990). *Atoms in Molecules: A Quantum Theory.* Oxford: Clarendon Press.
Bendeif, E.-E., Lecomte, C. & Dahaoui, S. (2009). *Acta Cryst.* B**65**, 59–67.
Blessing, R. H. (1987). *Cryst. Rev.* **1**, 3–58.
Bondi, A. (1964). *J. Phys. Chem.* **68**, 441–451.
Bouhmaida, N., Bonhomme, F., Guillot, B., Jelsch, C. & Ghermani, N. E. (2009). *Acta Cryst.* B**65**, 363–374.
Brünger, A. T. (1992). *Nature*, **355**, 472–475.
Clark, R. C. & Reid, J. S. (1995). *Acta Cryst.* A**51**, 887–897.
Clementi, E. & Roetti, C. (1974). *At. Data Nucl. Data Tables*, **14**, 177–478.
Coppens, P., Abramov, Y., Carducci, M., Korjov, B., Novozhilova, I., Alhambra, C. & Pressprich, M. R. (1999). *J. Am. Chem. Soc.* **121**, 2585–2593.
De Bondt, H. L., Blaton, N. M., Peeters, O. M., De Ranter, C. J. & Kjøller-Larsen, I. (1991). *The Application of Charge Density Research to Chemistry and Drug Design*, edited by G. A. Jeffrey & J. F. Piniella, NATO ASI Series (Series B: Physics), Vol. 250, pp. 341–349. New York: Plenum Press.
Domagała, S. & Jelsch, C. (2008). *J. Appl. Cryst.* **41**, 1140–1149.
Edwards, D. I. (1981). *Prog. Med. Chem.* **18**, 87–116.
Epstein, J., Ruble, J. R. & Craven, B. M. (1982). *Acta Cryst.* B**38**, 140–149.
Espinosa, E., Souhassou, M., Lachekar, H. & Lecomte, C. (1999). *Acta Cryst.* B**55**, 563–572.
Fournier, B., Bendeif, E.-E., Guillot, B., Podjarny, A., Lecomte, C. & Jelsch, C. (2009). *J. Am. Chem. Soc.* **131**, 10929–10941.
Grabowski, S. (2006). Editor. *Hydrogen Bonding – New Insights*, pp. 337–375. New York: Springer.
Guillot, B. (2010). *MoProViewer: a Molecular Viewer Dedicated to Charge Density Analysis*, Poster No. P19 presented at the French Cryst. Ass. AFC2010 (Strasbourg). 7–10 July 2010, http://www.crm2.uhp-nancy.fr/crm2/fr/labo/equipes/emqc/.
Guillot, B., Jelsch, C., Podjarny, A. & Lecomte, C. (2008). *Acta Cryst.* D**64**, 567–588.
Guillot, R., Muzet, N., Dahaoui, S., Lecomte, C. & Jelsch, C. (2001). *Acta Cryst.* B**57**, 567–578.
Guillot, B., Viry, L., Guillot, R., Lecomte, C. & Jelsch, C. (2001). *J. Appl. Cryst.* **34**, 214–223.
Hansen, N. K. & Coppens, P. (1978). *Acta Cryst.* A**34**, 909–921.
Herbst-Irmer, R., Henn, J. & Meindl, K. (2010). ECM, poster MS37-P04. Darmstadt, Germany.
Hernández-Trujillo, J. & Matta, C. F. (2007). *Struct. Chem.* **18**, 849–857.
Hirshfeld, F. L. (1976). *Acta Cryst.* A**32**, 239–244.
Hoser, A. A., Dominiak, P. M. & Woźniak, K. (2009). *Acta Cryst.* A**65**, 300–311.
Jelsch, C., Guillot, B., Lagoutte, A. & Lecomte, C. (2005). *J. Appl. Cryst.* **38**, 38–54.
Koch, U. & Popelier, P. L. A. (1995). *J. Chem. Phys.* **99**, 9747–9754.
Koritsanszky, T. (2006). *Hydrogen Bonding – New Insights*, edited by S. J. Grabowski, pp. 441–470. Berlin: Springer.
Koritsanszky, T. S. & Coppens, P. (2001). *Chem. Rev.* **101**, 1583–1627.
Kubicki, M. (2004*a*). *Acta Cryst.* C**60**, o255–o257.
Kubicki, M. (2004*b*). *J. Mol. Struct.* **698**, 67–73.
Kubicki, M. (2005). *J. Mol. Struct.* **743**, 209–215.
Kubicki, M., Borowiak, T., Dutkiewicz, G., Souhassou, M., Jelsch, C. & Lecomte, C. (2002). *J. Phys. Chem. B*, **106**, 3706–3714.

research papers

Kubicki, M., Borowiak, T., Suwiński, J. & Wagner, P. (2001). *Acta Cryst.* C**57**, 106–108.

Kubicki, M. & Wagner, P. (2007). *Acta Cryst.* C**63**, o454–o457.

Kubicki, M. & Wagner, P. (2008). *J. Mol. Struct.* **876**, 134–139.

Kuhs, W. F. (1992). *Acta Cryst.* A**48**, 80–98.

Kulda, J. & Hrdý, I. (2008). *Microbiol. Monogr.* **9**, 179–199.

Larson, A. C. & Von Dreele, R. B. (1994). *GSAS*. Los Alamos National Laboratory Report. Los Alamos National Laboratory, Los Alamos, USA.

Liebschner, D., Elias, M., Moniot, S., Fournier, B., Scott, K., Jelsch, C., Guillot, B., Lecomte, C. & Chabriere, E. (2009). *J. Am. Chem. Soc.* **13**, 7879–7886.

Macrae, C. F., Bruno, I. J., Chisholm, J. A., Edgington, P. R., McCabe, P., Pidcock, E., Rodriguez-Monge, L., Taylor, R., van de Streek, J. & Wood, P. A. (2008). *J. Appl. Cryst.* **41**, 466–470.

Madhavi, N. N. L., Katz, A. K., Carrell, H. L., Nangia, A. & Desiraju, G. R. (1997). *J. Chem. Soc. Chem. Commun.* pp. 1953–1954.

Madsen, A. Ø. (2006). *J. Appl. Cryst.* **39**, 757–758.

Mantina, M., Chamberlin, A. C., Valero, R., Cramer, C. J. & Truhla, D. G. (2009). *J. Phys. Chem. A*, **113**, 5806–5812.

Matta, C. F., Hernández-Trujillo, J., Tang, T. H. & Bader, R. F. W. (2003). *Chem. Eur. J.* **9**, 1940–1951.

Meindl, K., Herbst-Irmer, R. & Henn, J. (2010). *Acta Cryst.* A**66**, 362–371.

Munshi, P. & Row, T. N. G. (2005a). *J. Phys. Chem. A*, **109**, 659–672.

Munshi, P. & Row, T. N. G. (2005b). *Cryst. Rev.* **11**, 199–241.

Munshi, P. & Row, T. N. G. (2006). *Acta Cryst.* B**62**, 612–626.

Muzet, N., Guillot, B., Jelsch, C., Howard, E. & Lecomte, C. (2003). *Proc. Natl. Acad. Sci.* **100**, 8742–8747.

Oxford Diffraction (2009). *CrysAlis PRO*, Version 1.171.33.36d. Oxford Diffraction Ltd, Yarnton, England.

Paul, A. (2011). *J.Phys. Chem. A*. Submitted for publication.

Ranganathan, A., Kulkarni, G. U. & Rao, C. N. R. (2003). *J. Mol. Struct.* **656**, 249–263.

Sheldrick, G. M. (2008). *Acta Cryst.* A**64**, 112–122.

Sørensen, H. O., Stewart, R. F., McIntyre, G. J. & Larsen, S. (2003). *Acta Cryst.* A**59**, 540–550.

Stash, A. & Tsirelson, V. (2002). *J. Appl. Cryst.* **35**, 371–373.

Stewart, R. F. (1991). *The Application of Charge Density Research to Chemistry and Drug Design*, edited by G. A. Jeffrey & J. F. Piniella, NATO ASI Series (Series B: Physics), Vol. 250, pp. 63–101. New York: Plenum Press.

Toby, B. H. (2001). *J. Appl. Cryst.* **34**, 210–213.

Volkov, A., Macchi, P., Farrugia, L. J., Gatti, C., Mallinson, P., Richter, T. & Koritsánszky, T. (2006). *XD*2006, Revision 5.34. University of New York at Buffalo, NY, USA.

Wagner, P. & Kubicki, M. (2007). *Acta Cryst.* E**63**, o3083.

Wagner, P., Świerczek, K. & Kubicki, M. (2007). *Acta Cryst.* C**63**, o445–o447.

Wilson, A. J. C. (1992). Editor. *International Tables for Crystallography*, Vol. C, pp. 219–222. Dordrecht: Kluwer Academic Publishers.

Zhurova, E. A. & Pinkerton, A. A. (2001). *Acta Cryst.* B**57**, 359–365.

Zhurov, V. V., Zhurova, E. A., Stash, A. I. & Pinkerton, A. A. (2011). *Acta Cryst.* A**67**, 160–173.